Numerical Simulation of Polymer Injection in Turbulent Flow Past a Circular Cylinder

David Richter
e-mail: drichter@stanford.edu

Eric S. G. Shaqfeh
e-mail: esgs@stanford.edu

Gianluca Iaccarino
e-mail: jops@stanford.edu

Dept. of Mechanical Engineering,
Stanford University,
Stanford, CA 94305

Using a code developed to compute high Reynolds number viscoelastic flows, polymer injection from the upstream stagnation point of a circular cylinder is modeled at Re = 3900. Polymer stresses are represented using the FENE-P constitutive equations. By increasing polymer injection rates within realistic ranges, significant near wake stabilization is observed. Rather than a turbulent detached shear layer giving way to a chaotic primary vortex (as seen in Newtonian flows at high Re), a much more coherent primary vortex is shed, which possesses an increased core pressure as well as a reduced level of turbulent energy. [DOI: 10.1115/1.4004960]

1 Introduction

It is well-established that the injection of dilute solutions of polymers into turbulent flows produces large effects on the underlying fluid dynamics and that these effects can be exploited for numerous engineering purposes. Perhaps the most common example of this is in the area of turbulent drag reduction, where skin friction drag over flat surfaces can be reduced up to 80% in the presence of polymer additives [1–3]. Beyond drag reduction, however, we have recently shown that viscoelasticity can significantly alter the flow within a bluff body wake, effectively delaying the Newtonian modes of turbulent transition [4–6]. Specifically, we investigated the flow of homogeneous dilute polymer solutions at large Reynolds numbers ($Re = 3900$), and viscoelasticity was found to stabilize the shear layer immediately behind the surface of the cylinder, causing the wake to appear qualitatively similar to the Newtonian structure observed at much lower Reynolds numbers. It is therefore the purpose of this brief to expand these studies to include the modeling of inhomogeneous polymer concentrations (i.e. model polymer injection rather than assume an "ocean of polymer"), and to relate the findings to relevant engineering applications.

2 Model

In general, the dimensional mass and momentum conservation equations for a fluid in the presence of an additional polymeric stress are shown below:

$$\frac{\partial u_j}{\partial x_j} = 0 \tag{1}$$

$$\frac{\partial u_i}{\partial t} + u_j \frac{\partial u_i}{\partial x_j} = -\frac{1}{\rho}\frac{\partial p}{\partial x_i} + \frac{1}{\rho}\frac{\partial}{\partial x_j}\left(\mu_s \frac{\partial u_i}{\partial x_j}\right) + \frac{1}{\rho}\frac{\partial \tau_{ij}^p}{\partial x_j} \tag{2}$$

where μ_s is the dynamic viscosity of the solvent and ρ is the fluid density. For this study, the molecular-based FENE-P model is used, which provides a continuum representation of additional polymeric stress τ_{ij}^p throughout the entire flow field. In its dimensional form, this stress is given by:

$$\tau_{ij}^p = 2n_p kT\beta_d^2 \frac{c_{ij}}{1 - c_{kk}/L^2} - n_p kT\delta_{ij} \tag{3}$$

In this form, c_{ij} represents the polymer conformation (the average dyadic product of the dumbbell end-to-end vector), which satisfies its own evolution equation, L is the maximum polymer extensibility, n_p refers to the local polymer number density, k is Boltzmann's constant, T is the temperature, and β_d is a molecular property based on the size and number of Kuhn steps along an individual polymer contour. Additionally, the polymer contribution μ_p to the total solution viscosity $\mu_T = \mu_s + \mu_p$ is given by:

$$\mu_p = n_p kT\lambda \tag{4}$$

where λ is the polymer relaxation time. Now, by making Eqs. (1), (2) dimensionless using the cylinder diameter D as the relevant length scale, the convective time U_∞/D as the time scale, and the total solution viscosity $\mu_{T,0}$ at the injector location as the viscosity scale, the dimensionless governing equations, including that for the conformation tensor c_{ij} are shown below:

$$\frac{\partial u_j}{\partial x_j} = 0 \tag{5}$$

$$\begin{aligned}\frac{\partial u_i}{\partial t} + u_j \frac{\partial u_i}{\partial x_j} = &-\frac{\partial p}{\partial x_i} + \frac{1}{Re}\frac{\partial}{\partial x_j}\left[(1 - (1-\beta_0)\phi)\frac{\partial u_i}{\partial x_j}\right] \\ &+ \frac{1}{WiRe}\frac{\partial}{\partial x_j}\left[((1-\beta_0)\phi)\left(\frac{c_{ij}}{1 - c_{kk}/L^2} - \delta_{ij}\right)\right]\end{aligned} \tag{6}$$

$$\frac{\partial c_{ij}}{\partial t} + u_k \frac{\partial c_{ij}}{\partial x_k} = c_{ik}\frac{\partial u_j}{\partial x_k} + c_{kj}\frac{\partial u_i}{\partial x_k} - \frac{1}{Wi}\left(\frac{c_{ij}}{1 - \frac{c_{kk}}{L^2}} - \delta_{ij}\right) \tag{7}$$

In Eqs. (5)–(7), the Weissenberg number is defined as $Wi = \lambda U_\infty/D$; the Reynolds number is based on the total solution viscosity at the injection point, $Re = \rho U_\infty D/\mu_{T,0}$; $\beta_0 = \mu_{s,0}/(\mu_{s,0} + \mu_{p,0})$ is the viscosity ratio at the injection surface; and ϕ is the local polymer concentration in the interior of the domain, normalized by the number density of injected solution: $\phi = n_p/n_{p,0}$. Therefore, upon specifying an injection viscosity ratio β_0, the solution of the inhomogeneous equations also requires knowledge of the local polymer concentration ϕ. Note that $\beta_0 = 1$ would result in a pure solvent injection.

Computing the polymer concentration ϕ involves solving a convection-diffusion conservation equation:

$$\frac{\partial \phi}{\partial t} + u_j \frac{\partial \phi}{\partial x_j} = \frac{1}{Pe}\frac{\partial}{\partial x_j}\left[\frac{\partial n_p}{\partial x_j} - \frac{\partial \tau_{jk}^p}{\partial x_k}\right] \tag{8}$$

where Pe refers to the Péclet number of the polymer components and can be written in terms of a Reynolds number and Schmidt number (the ratio of momentum to scalar diffusivity, $Sc = \nu/\Gamma_\phi$): $Pe = ReSc$. Molecular diffusivities of aqueous solutions of polymers are very small, giving rise to Schmidt numbers that are $O(10^5)$ [7,8]; thus, advection dominates the transport of polymer concentration. As a result, the stress diffusion term $\partial \tau_{jk}^p/\partial x_k$ is neglected and a Schmidt number of 10 is used for the polymer concentration in order to limit the grid resolution requirement (maximum that can be used without incurring numerical instabilities).

Contributed by the Fluids Engineering Division of ASME for publication in the JOURNAL OF FLUIDS ENGINEERING. Manuscript received June 1, 2011; final manuscript received August 24, 2011; published online September 27, 2011. Assoc. Editor: Hassan Peerhossaini.

3 Numerical Method

To solve Eqs. (5)–(8), the code described in our previous works was utilized [4,5], and only a brief description will be provided here.

The numerical method is based on a spatially second-order, unstructured finite-volume formulation and is stepped in time with a second-order Crank-Nicholson scheme. Convective velocity derivatives are computed using central differencing, while scalar (c_{ij}, ϕ) advective derivatives are computed using quadratic upwinding for convective kinematics (QUICK). Incompressibility is enforced via a fractional step approach, where first a velocity field which satisfies the momentum equation is found, then a pressure Poisson system is solved, and finally the velocity field is then corrected to be discretely divergence-free.

The conformation tensor components c_{ij} are computed prior to solving the momentum equations within a time step, and velocity gradients which appear on the right side of Eq. (7) are computed using a Green-Gauss formulation:

$$\frac{\partial u_i}{\partial x_j} \approx \frac{1}{V}\int_{\partial\Omega} u_i n_j dA \approx \frac{1}{V}\sum_f u_i n_j A_f \tag{9}$$

where n_j is the face-normal unit vector and V is the cell volume. Similarly, the extra polymer stress term that appears in Eq. (6) is treated as a volumetric source term with gradients computed with Eq. (9).

As described in Richter et al. [4], an extra step is taken within each time step to guarantee polymer stretch boundedness (i.e. the trace c_{kk} must always be limited by L^2). Furthermore, due to numerical limitations, artificial diffusivity for c_{ij} is introduced at a Schmidt number of $Sc_c = 0.77$. Values of Sc_c of this order have been seen previously to have minimal effect on computed quantities [4,9].

4 Problem Definition

The flow that is investigated is flow past a circular cylinder at $Re = 3900$, with injection of polymer solution from a 30° wedge along the entire span of the cylinder. Figure 1 illustrates this schematically. It should be noted that the wedge angle of 30° used in this case is somewhat arbitrary. The goal was merely to maintain realistic values of injection flow rates without inducing large perturbations to the upstream flow through the injection velocity.

Injection is represented by prescribing a specified wall-normal velocity u_{inj} in addition to a normalized concentration of $\phi = 1$ on the injector surface. Elsewhere, the cylinder surface is no-slip for the fluid velocity, and a no-flux condition is used for c_{ij} and ϕ.

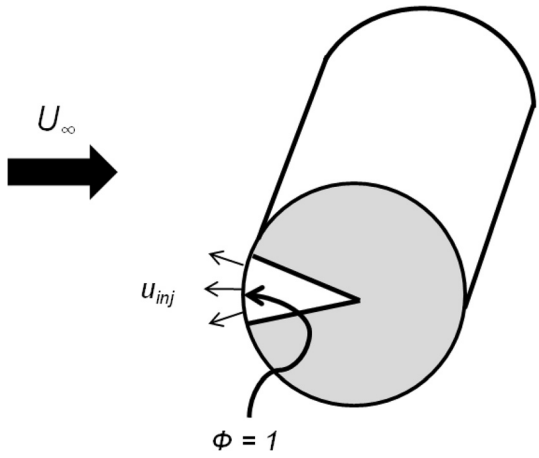

Fig. 1 Schematic of injector, showing region of prescribed normal injector velocity u_{inj} and constant normalized concentration $\phi = 1$

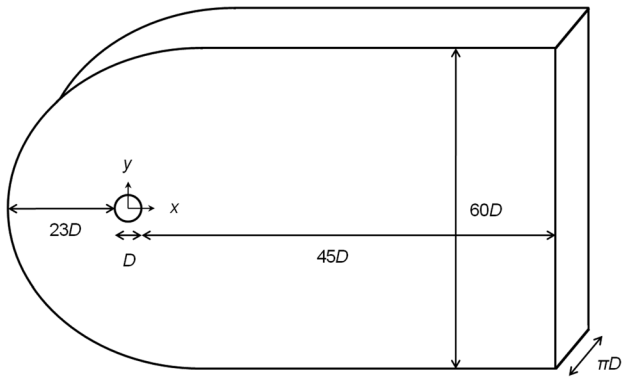

Fig. 2 Schematic of the computational domain

The entire computational domain is illustrated in Fig. 2. The domain extends $23D$ radially upstream and $45D$ downstream of the cylinder in the xy plane. A free-stream velocity of $U_\infty = [1, 0, 0]$, a near-equilibrium polymer conformation of $c_{ij} = \delta_{ij}$, and a polymer concentration of $\phi = 0$ is specified along the entire domain far-field (the curved inlet as well as the horizontal boundaries above and below the wake). Outlet convective boundary conditions are used for all quantities at the vertical exit boundary.

The computational mesh is unstructured, and has a minimum spacing at the cylinder surface of $\Delta r = 0.0015D$ and $\Delta\theta = 0.027D$. Over the span of πD, 64 elements are used in the z -direction. Overall, there are 3.6×10^6 cells in the entire mesh. Convergence tests have been performed and are described elsewhere [4,6].

For this study, two normalized injection rates were compared: $u_{inj} = 0.1$ and $u_{inj} = 0.3$ (each normalized by U_∞), which correspond to dimensionless flow rates of $Q = 0.085$ and $Q = 0.26$, respectively (flow rate nondimensionalized by $U_\infty D^2$). Furthermore, for all cases considered, the Weissenberg number is set as $Wi = 10$, the injector viscosity ratio is prescribed as $\beta_0 = 0.1$, and the polymer extensibility is set to $L = 50$. For homogeneous polymer concentrations at $Re = 3900$, the rheological parameters $Wi = 10$ and $L = 50$ have been observed to have a profound impact on the structure of the wake [6].

Finally, it should be noted that the injection flow rates used are in the same range as in two of the few experimental polymer injection studies done for flow over a cylinder at lower Reynolds numbers. Cadot and Lebey [10] quote an injection rate between 0 and 2.5 L/hr, when scaled by their value of $U_\infty D^2$ results in a maximum flow rate of $Q = 0.72$, which is actually higher than the largest used in the present study. Furthermore, Cadot and Kumar [11], while they do not indicate the injection flow rates used, quote a ratio of injector velocity to free stream velocity of $0 < u_{inj}/U_\infty < 0.6$, which is also very close to the ranges used presently. Both of these studies were performed for a Reynolds number around $Re = 190$.

5 Results

Figure 3 shows instantaneous surfaces of spanwise vorticity, $\omega_z = \pm 9.0$, for a Newtonian case and the viscoelastic cases for the two specified injection rates.

Clearly, the injection of polymeric additives from the upstream face of the cylinder can alter the flow, even at low rates of injection. As this rate is increased, the shear layer is nearly completely stabilized, and a spanwise vortex is shed with much more coherency than for the Newtonian case. It was argued in Richter et al. [6] that at such high Reynolds numbers, stabilization of the detached shear layer was a key component in assessing the degree of stabilization that viscoelasticity provides. This would indicate that extra polymeric stresses are only needed in the region of the shear layer, which is evidenced by Fig. 3.

To further confirm this idea, velocity energy spectra were taken within the shear layer as well as downstream and compared to

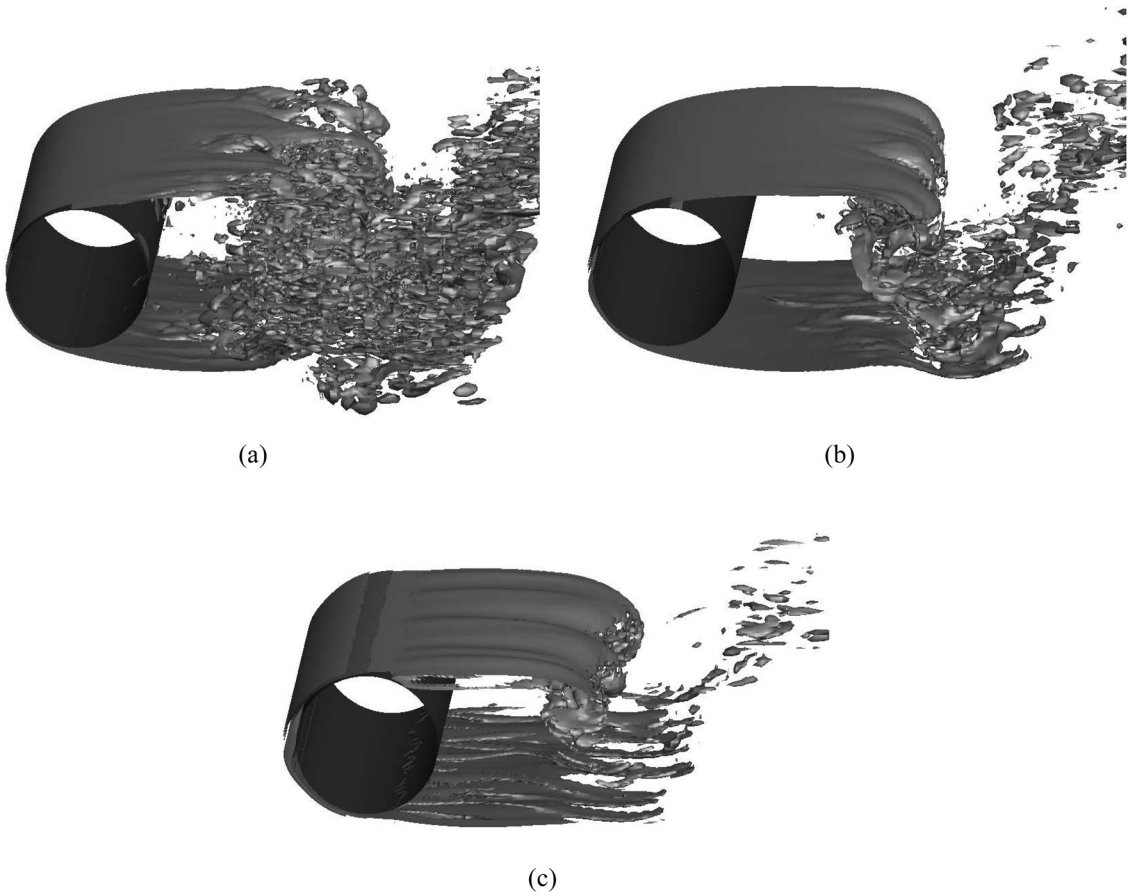

Fig. 3 Surfaces of instantaneous vorticity $\omega_z = \pm 9.0$ for: (*a*) Newtonian flow; (*b*) injection velocity $u_{inj} = 0.1$ ($Q = 0.0853$); (*c*) injection velocity $u_{inj} = 0.3$ ($Q = 0.256$). Injection cases are viscoelastic with $Wi = 10$, $L = 50$, and $\beta_0 = 0.1$.

both the Newtonian and homogeneous cases. Figure 4 shows the spanwise-averaged velocity spectra $\bar{E}_{22}$ taken at a point within the shear layer. Within the shear layer, Newtonian flow exhibits a frequency peak due to the Kelvin-Helmoltz instability, which develops in the shear layer at these Reynolds numbers [12,13], and this is seen clearly in Fig. 4 at $f/f_{St} \approx 6$. With even small injection rates, this peak vanishes, indicating a stabilization of this Kelvin-Helmoltz instability, while the shear layer still maintains more transverse energy content than the homogeneous case.

What is more interesting is seen in streamwise energy spectra taken much further downstream, at $x/D = 7.0$ at the wake centerline. This is shown in Fig. 5. At this point downstream, which contains near-zero concentrations of polymer solution, the energy contained in large scales for both injection cases is seen to be

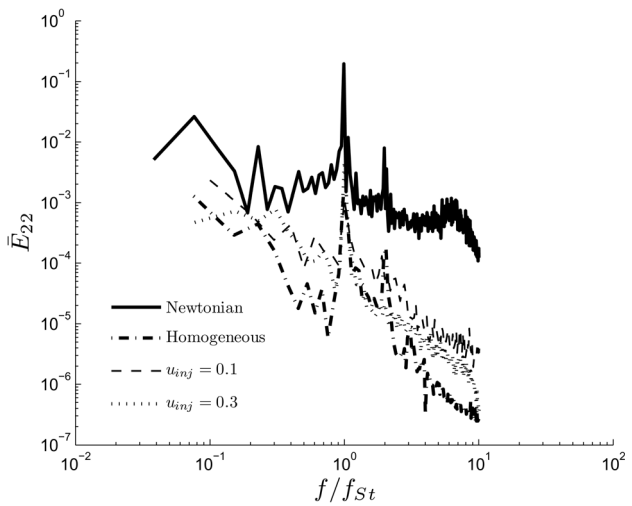

Fig. 4 Energy spectra $\bar{E}_{22}$ taken within the shear layer. Viscoelastic computations are at $\beta_0 = 0.1$, $Wi = 10$, and $L = 50$. Homogeneous simulation at $Wi = 10$, $L = 50$, and $\beta = 0.9$. Frequency normalized with Strouhal frequency.

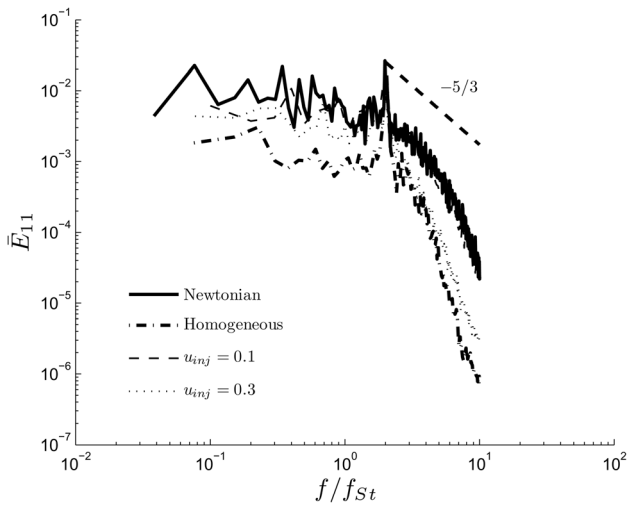

Fig. 5 Energy spectra $\bar{E}_{11}$ measured at $y/D = 0$, $x/D = 7.0$. Viscoelastic computations are at $\beta_0 = 0.1$, $Wi = 10$, and $L = 50$. Homogeneous simulation at $Wi = 10$, $L = 50$, and $\beta = 0.9$. Frequency normalized with Strouhal frequency.

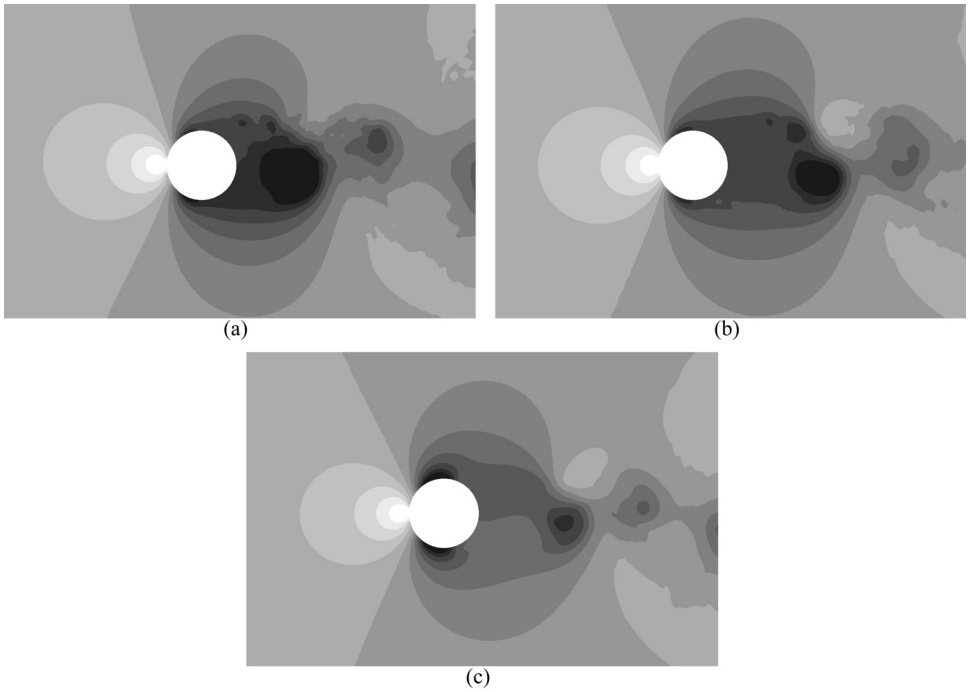

Fig. 6 Contours of spanwise-averaged reference pressure $\bar{p}$ at an instant in time for the cases of: (*a*) Water injection at $u_{inj} = 0.3$; (*b*) Polymer injection at $u_{inj} = 0.1$, $Wi = 10$, $L = 50$, $\beta_0 = 0.1$; and (*c*) Polymer injection at $u_{inj} = 0.3$, $Wi = 10$, $L = 50$, $\beta_0 = 0.1$. Scale is the same for all three figures with 10 contours between $-0.6 < \bar{p} < 0.4$. Dark colors are for low pressure. Light colors are for high pressure.

diminished compared to the Newtonian case but still not as reduced as the homogeneous case. At small scales (higher frequency content), however, the high injection rate $u_{inj} = 0.3$ results in energy content nearly matching that of the homogeneous case, while the lower injection rate matches that of the Newtonian flow. This suggests that while both rates of injection qualitatively seem to stabilize the shear layer (cf. Fig. 3), the large injection rate provides sufficient upstream influence that then greatly reduces small-scale turbulent energy downstream despite there being no significant polymer stresses at these downstream locations. This is contrary to the low injection rate, which is not sufficient to prevent the far wake from gaining nearly as much turbulent energy as the Newtonian flow.

6 Application

While turbulent drag reduction is perhaps the most citied function of polymer injection into turbulent flow, other interesting applications exist which could be benefitted through numerical simulation. One such example is suppression of propeller tip vortex cavitation, where dilute solutions of polymer are injected in order to prevent cavitation from occurring within the strong vortex that develops from the propeller tip [14–16]. By affecting the rollup process, a larger-radius vortex was seen experimentally to develop in the presence of polymer injection, with a higher core pressure than for the same injection rates of water. This higher pressure then delayed the inception of tip vortex cavitation. Although the geometry is clearly different for the case of flow over a cylinder, Fig. 6 shows contours of spanwise-averaged reference pressure (at a certain instant in time) within the cylinder wake for the two viscoelastic injection cases, as well as a case of water injection at the larger rate ($u_{inj} = 0.3$). The spanwise-average minimum pressure within a newly developed core increases dramatically with polymer injection, rising from $\bar{p}_{\min} \approx -1.0$ for water injection to $\bar{p}_{\min} \approx -0.52$ for polymer injection at $u_{inj} = 0.3$. From Fig. 6, it appears that the same phenomenon is occurring: the rollup of primary vortices is significantly altered in the presence of sufficient viscoelastic influence, and this in turn weakens the strength of the vortex core, which increases the core pressure.

7 Conclusions

A numerical model for polymer injection was utilized to study the effects which inhomogeneous concentrations of viscoelasticity has on flow over a circular cylinder at $Re = 3900$. It was observed that many of the same effects seen for homogeneous polymer concentrations [6] could be obtained with injection from the upstream face of the cylinder, including a suppression of the Kelvin-Helmoltz instability which forms in the detached shear layer for Newtonian flows at the same Reynolds number, as well as a reduction in turbulent energy in the far wake. It was then demonstrated that this type of analysis would be beneficial for applications of polymer injection beyond those of turbulent drag reduction, including tip vortex cavitation suppression.

Acknowledgment

This research has been funded in part by a KAUST research grant under the KAUST-Stanford Academic Excellence Alliance program. Additionally, the authors acknowledge the following award for providing computing resources that have contributed to the research results reported within this paper: MRI-R2: Acquisition of a Hybrid CPU/GPU and Visualization Cluster for Multidisciplinary Studies in Transport Physics with Uncertainty Quantification. This award is funded under the American Recovery and Reinvestment Act of 2009 (Public Law 111-5).

References

[1] Sureshkumar, R., Beris, A. N., and Handler, R. A., 1997, "Direct Numerical Simulation of the Turbulent Channel Flow of a Polymer Solution," Phys. Fluids, **9**(3), pp. 743–755.
[2] White, C., and Mungal, G., 2008, "Mechanics and Prediction of Turbulent Drag Reduction With Polymer Additives," Annu. Rev. Fluid Mech., **40**, pp. 235–256.
[3] Winkel, E. S., Oweis, G. F., Vanapalli, S. A., Dowling, D. R., Perlin, M., Soloman, M. J., and Ceccio, S. L., 2009, "High-Reynolds-Number Turbulent

Boundary Layer Friction Drag Deduction From Wall-Injected Polymer Solutions," J. Fluid Mech., **621**, pp. 259–288.
[4] Richter, D., Iaccarino, G., and Shaqfeh, E. S. G., 2010, "Simulations of Three-Dimensional Viscoelastic Flows Past a Circular Cylinder at Moderate Reynolds Numbers," J. Fluid Mech., **651**, pp. 415–442.
[5] Richter, D., Shaqfeh, E. S. G., and Iaccarino, G., 2011, "Floquet Stability Analysis of Viscoelastic Flow Over a Cylinder," J. Non-Newtonian Fluid Mech., **166**, pp. 554–565.
[6] Richter, D., Iaccarino, G., and Shaqfeh, E. S. G., 2011, "Effects of Viscoelasticity in the High Reynolds Number Cylinder Wake," J. Fluid Mech., submitted.
[7] Dimitropoulos, C. D., Dubief, Y., Shaqfeh, E. S. G., and Moin, P., 2006, "Direct Numerical Simulation of Polymer-Induced Drag Reduction in Turbulent Boundary Layer Flow of Inhomogeneous Polymer Solutions," J. Fluid Mech., **566**, pp. 153–162.
[8] Beris, A. N., and Edwards, B. J., 1994, *Thermodynamics of Flowing Systems With Internal Microstructure*, Oxford University Press, New York.
[9] Dubief, Y., Terrapon, V. E., White, C. M., Shaqfeh, E. S. G., Moin, P., and Lele, S. K., 2005, "New Answers on the Interaction Between Polymers and Vortices in Turbulent Flows," Flow, Turbul. Combust., **74**(4), pp. 311–329.
[10] Cadot, O., and Lebey, M., 1998, "Shear Instability Inhibition in a Cylinder Wake by Local Injection of a Viscoelastic Fluid," Phys. Fluids, **11**(2), pp. 494–496.
[11] Cadot, O., and Kumar, S., 2000, "Experimental Characterization of Viscoelastic Effects on Two- and Three-Dimensional Shear Instabilities," J. Fluid Mech., **416**, pp. 151–172.
[12] Bloor, M. S., 1964, "The Transition to Turbulence in the Wake of a Circular Cylinder," J. Fluid Mech., **19**, pp. 290–304.
[13] Prasad, A., and Williamson, C. H. K., 1997, "The Instability of the Shear Layer Separating From a Bluff Body," J. Fluid Mech., **333**, pp. 375–402.
[14] Chahine, G. L., Frederick, G. F., and Bateman, R. D., 1993, "Propeller Tip Vortex Cavitation Suppression Using Selective Polymer Injection," J. Fluids Eng., **115**, pp. 497–503.
[15] Fruman, D. H., Pichon, T., and Cerrutti, P., 1995, "Effect of a Drag-Reducing Polymer Solution Ejection on Tip Vortex Cavitation," J. Mar. Sci. Technol., **1**, pp. 13–23.
[16] Yakushiji, R., Chang, N. A., and Ceccio, S. L., 2008, "Tip Vortex Cavitation Suppression by Water and Polymer Injection," 27th Symposium on Naval Hydrodynamics, Seoul, Korea, October 5–10, 2008.